BERKELEY LAB

Energy Analysis Division

Source-Resolved Inversion of Elemental Carbon Emissions in California Using Log-Space Bayesian Inference

Jie Zhang[1], Ling Jin[1], Xiaodan Xu[1], Soroush E. Neyestani[2], Xinyi Zhang[2], Tin Ho[3], Jiachen[4], Zhang[2], James Butler4, Chelsea V. Preble[4], Thomas W. Kirchstetter[1], [4], Qi Ying[5], Zichong Chen[6], [5] Anna Spurlock[1], Hanna Breunig[1]

[1] Energy Analysis Division, Lawrence Berkeley National Laboratory, Berkeley, CA 94720, USA 7
[2] Department of Civil and Environmental Engineering, University of Southern California, Los 8 Angeles, CA 90089, USA 9
[3] Science IT Department, Lawrence Berkeley National Laboratory, Berkeley, CA 94720, USA 10
[4] Department of Civil and Environmental Engineering, University of California, Berkeley, 11 Berkeley, CA 94720, USA 12
[5] Division of Environment and Sustainability, Hong Kong University of Science and Technology, 13 Hong Kong 999077, China 14
[6] Thrust of Carbon Neutrality and Climate Change, Hong Kong University of Science and 15 Technology, Guangzhou 511453, China

June 2026

This is a pre-print version of an article published in ACS ES&T Air.
DOI: https://doi.org/10.1021/acsestair.6c00105

This work was supported by the DOE Office of Clean Energy Demonstrations under Lawrence Berkeley National Laboratory Contract No. DE-AC02-05CH11231.

Disclaimer

Copyright Notice

Source-Resolved Inversion of Elemental Carbon Emissions in California Using Log-space Bayesian Inference

Jie Zhang[1,*], Ling Jin[1,*], Xiaodan Xu[1], Soroush E. Neyestani[2], Xinyi Zhang[2], Tin Ho[3], Jiachen Zhang[2], James Butler[4], Chelsea V. Preble[4], Thomas W. Kirchstetter[1,4], Qi Ying[5], Zichong Chen[6], Anna Spurlock[1], Hanna Breunig[1]

[1] Energy Analysis Division, Lawrence Berkeley National Laboratory, Berkeley, CA 94720, USA
[2] Department of Civil and Environmental Engineering, University of Southern California, Los Angeles, CA 90089, USA
[3] Science IT Department, Lawrence Berkeley National Laboratory, Berkeley, CA 94720, USA
[4] Department of Civil and Environmental Engineering, University of California, Berkeley, Berkeley, CA 94720, USA
[5] Division of Environment and Sustainability, Hong Kong University of Science and Technology, Hong Kong 999077, China
[6] Thrust of Carbon Neutrality and Climate Change, Hong Kong University of Science and Technology, Guangzhou 511453, China

[*]Correspondences: Jie Zhang: jzhang9@lbl.gov, Ling Jin: ljin@lbl.gov

Abstract

Elemental carbon (EC), operationally quantified by thermal-optical analysis, is widely used as a proxy for black carbon (BC) relevant to short term climate forcing and public health. Current EC emission inventories remain highly uncertain, with persistent discrepancies between bottom-up and top-down estimates. In this study, we develop a source-resolved, log-space Bayesian inversion framework applied to estimate California's statewide EC emissions in 2019. By integrating surface EC measurements from the EPA's Air Quality System network with high-resolution source contributions simulated by a chemical transport model, we identify a one-third underestimation in the existing statewide EC inventory, requiring an increase of the total from a prior of 8.58 [5.49–13.75] Gg yr^{-1} to a posterior estimate of 12.78 [10.71–15.37] Gg yr^{-1}. This discrepancy is primarily driven by substantial underestimations in the power & industrial and off-road mobile sectors. Furthermore, population-weighted exposure analysis reveals a marked sectoral divergence between emission mass and health burden: off-road mobile sources dominate both emissions and exposure, accounting for 31% of statewide exposure, while residential wood combustion contributes 26% of total exposure despite comprising only 19% of total emissions, due to its source proximity to population. These findings underscore the need to update sector-specific EC speciation profiles and demonstrate that mitigation strategies targeting off-road mobile sources and residential wood combustion are critical for reducing EC-related health impacts in California.

Keywords

Bayesian inversion; Logarithmic space; Elemental carbon; EC mass fraction; Source-resolved

Introduction

Elemental carbon (EC), a primary constituent of fine particulate matter ($PM_{2.5}$), is commonly emitted from fuel combustion and routinely reported in the emission inventory. EC is operationally defined as the thermally measured fraction of carbonaceous aerosols in regulatory monitoring networks, such as the US EPA's Air Quality System (AQS).[1,2] In studies of atmospheric warming and public health,[3,4] EC is widely used as a proxy for black carbon (BC), a potent short-lived climate pollutant (SLCP) that affects radiative forcing[5–8] and is linked to respiratory and cardiovascular diseases, premature mortality, and other adverse health outcomes, particularly in densely populated regions.[9–14] Consequently, EC mitigation offers valuable co-benefits for air quality, public health, and near-term climate stabilization. In California, where diverse anthropogenic emissions intersect with large population centers, quantifying EC sources and their contributions to population exposure is therefore essential for informed policy development.

Accurate quantification of EC emissions remains challenging. Bottom-up emission estimates are subject to substantial uncertainties arising from uncertain emission factors or speciation profiles, incomplete activity data, and the evolving nature of source sectors such as fleet turnover.[15,16] To address these limitations, ambient observations are used in top-down approaches to inversely constrain the EC emissions.[17,18] These top-down approaches, which incorporate remote sensing data and ground-based measurements, have consistently revealed systematic underestimations in current bottom-up EC inventories.[19–23] For example, Cohen and Wang [19] developed a global-scale Kalman Filter-based inversion of EC emissions using observations of column absorption, surface concentration, and near-surface local absorption from several monitoring networks, and found that commonly used inventories substantially underestimate EC emissions. Regionally, Wang et al.[20] found that the EC emissions over China were ~1.8 times higher than the bottom-up inventories. Mao et al.[21] applied GEOS-Chem adjoint model to estimate EC emissions in the Western US, revealing results nearly twice those reported in bottom-up inventories. While these studies provide insights into global and regional EC emission biases, to our knowledge, no study has implemented source-resolved inversion frameworks capable of attributing these discrepancies to individual source sectors.

The contribution of EC emission source sectors, however, varies significantly by scale and region. Globally, residential combustion, predominantly driven by solid biofuel use, represents the largest anthropogenic EC source, whereas on-road transportation constitutes the dominant sector in developed countries.[24–26] In the US, a bottom-up inventory indicates that transportation-related sources (e.g., diesel and gasoline engines) account for over 50% of anthropogenic EC emissions, followed by industrial sources at 22%.[27] In California specifically, the 2013 California Air Resource Board (CARB) SLCP inventory identifies off-road mobile sources as the largest sector (46%), followed by on-road diesel (18%), residential wood combustion (15%), and fuel combustion/industrial activities (14%). Notably, California's aggressive regulations have driven dramatic reductions in on-road diesel emissions and shift the state's source dominance toward the off-road sector.[28]

In this study, we develop and implement a logarithmic Bayesian inversion framework that integrates observation networks with the state-of-art chemical transport simulations to constrain EC emissions in California. While prior research has primarily focused on identifying discrepancies in total emissions, our approach reconciles inventories with measured surface concentrations to isolate and correct source-specific biases, enabling more reliable source attribution analysis. Source-receptor relationships are derived from the source-resolved regional chemical transport model (CTM) simulations at a 4-km resolution across California. The inversion framework constrains and validates EC emissions in California using surface EC measurements from the US EPA's AQS network. By operating in logarithmic space, the inversion effectively mitigates heteroscedasticity, ensuring more robust and stable source-resolved estimates.

Methods

Observation data

Daily EC observations (Parameter Code 88321 and 88380) were obtained from the EPA's AQS database.[29] These measurements were analyzed via thermal-optical reflectance (TOR) using various analytical protocols (Table S1). At monitoring sites where multiple measurement techniques were co-located, priority was given to the observations using the IMPROVE (Interagency Monitoring of PROtected Visual Environments) analytical protocol (Method Code 805). To ensure consistency across networks, EC observations (Method Code 838) reported by the Chemical Speciation Network (CSN) were adjusted by a factor of 0.79. The adjustment accounts for systematic discrepancies identified from the comparison of EC measurements with IMRPOVE_A and CSN protocols at a shared monitoring site (Figure S1).[30,31] No adjustments were applied to the measurements from non-EPA's monitoring sites (primarily managed by CARB or local research institutes) due to lack of protocol-specific bias adjustment studies as references. Additionally, a sensitivity analysis withholding these non-EPA data streams from the inversion yielded negligible differences in the posterior emission estimates, demonstrating the robustness of our baseline model constraints (see Figure S13). Collectively, there are 34 EC measurement sites across California, as shown in Figure 1, providing spatially comprehensive coverage suitable for model evaluation and subsequent inversion.

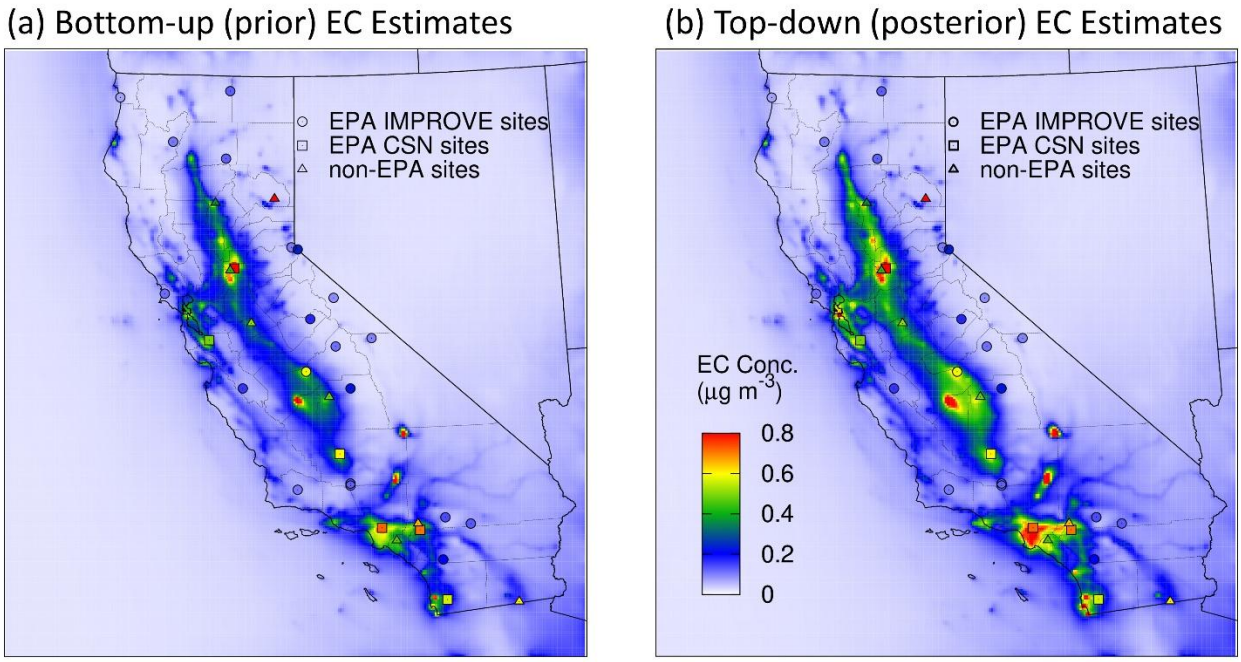

Figure 1. Modeling domain and spatial distribution of monitoring sites. The background color represents CMAQ-modeled annual average surface EC concentrations using (a) bottom-up (prior) emissions and (b) top-down (posterior) emissions. Monitoring site locations are overlaid as points color-coded to their corresponding annual average observed EC concentrations for model-observation comparison, including IMPROVE (circles, n = 20), CSN (squares, n = 6), and non-EPA (triangles, n = 8) sites.

Prior emission inventory

The prior emission inventory for anthropogenic sources was provided by the CARB by source categories and processed for the modeling year 2019. For the sectors other than on-road, emissions were taken from the most recent CARB's 2020 anthropogenic inventory, and processed with the Sparse Matrix Operator Kernel Emissions (SMOKE) system to produce gridded, hourly, speciated emissions by sector.[32] These sector-specific gridded emissions were then adjusted to 2019 levels using sector- and county-level scaling factors based on the ratio of annual emissions reported from the California Emission Projection Analysis Model (CEPAM) v1.04 for 2019 versus 2020. Since CARB's 2020 emission inventory did not account for COVID-related activity changes, no additional COVID-specific adjustment was applied. In contrast, on-road mobile source emissions were obtained directly for 2019 and spatiotemporally allocated using the Emissions Spatial and Temporal Allocator (ESTA)[33] to provide a high-fidelity representation of vehicle activity and emission patterns.

All anthropogenic sources were categorized into 7 primary sectors (as defined below) based on the EC emission signatures for the inversion analysis. A summary of total prior emissions for EC and primary $PM_{2.5}$ (pri-$PM_{2.5}$) by sector is provided in Table S2.

1. Power & industrial: includes area and point source emissions from power generation, petroleum production, and diverse industrial processes.
2. Off-road mobile: includes non-road engines and equipment, such as construction machinery, agricultural equipment, aircraft, locomotives, and marine vessels.
3. Residential wood combustion: accounts for emissions from woodstoves, wood inserts, and fireplaces primarily used for heating.
4. Light-duty vehicles: includes passenger cars and light-duty trucks, which mostly utilize gasoline engines. This sector also includes non-exhaust particles from brake and tire wear.
5. Heavy-duty vehicles: includes medium- and heavy-duty trucks and buses. These are predominantly diesel-powered and also include associated non-exhaust particles from brake and tire wear.
6. Fires: includes prescribed burning, and structural and automotive fires, distinct from wildfires.
7. Miscellaneous: includes all other anthropogenic activities that are not categorized elsewhere, such as waste disposal, residential and commercial cooking, and paved/unpaved road dust.

Biogenic emissions were estimated using the CMAQ in-line Biogenic Emission Inventory System (BEIS), which calculates hourly emissions based on simulated meteorology and land-cover data. Notably, wildfires were excluded from this analysis, as there were few significant wildfire events in California during 2019 based on California fire incidents database [34], and it is not within our current research scope.

Source-resolved chemical transport model

To facilitate source attribution for a sector-resolved emission inversion, an efficient source apportionment technique for EC using source-tagged tracers[35,36] was implemented in the Community Multiscale Air Quality (CMAQ) model v5.5.[37] For each emission sector, distinct non-reactive tracers for EC were integrated into the model's aerosol species list. These tracers undergo the same transport and removal processes as other non-reactive PM components, ensuring consistency with modeled aerosol dynamics. To prevent these additional species from artificially affecting particle size distributions or removal kinetics, tracer emission rates were scaled by a factor of 10^{-5} relative to the sector-specific prior EC emissions. The absolute sector-specific concentrations were subsequently recovered during postprocessing by applying a scaling factor of 10^5 to the resulting tracer concentrations, providing precise estimates of each sector's contribution to the total mass of EC. EC concentrations attributable to individual sectors exhibit distinct spatial patterns as shown in Figure 2, which will be further reconciled with the observed EC concentrations to derive sector resolved posterior emission estimates.

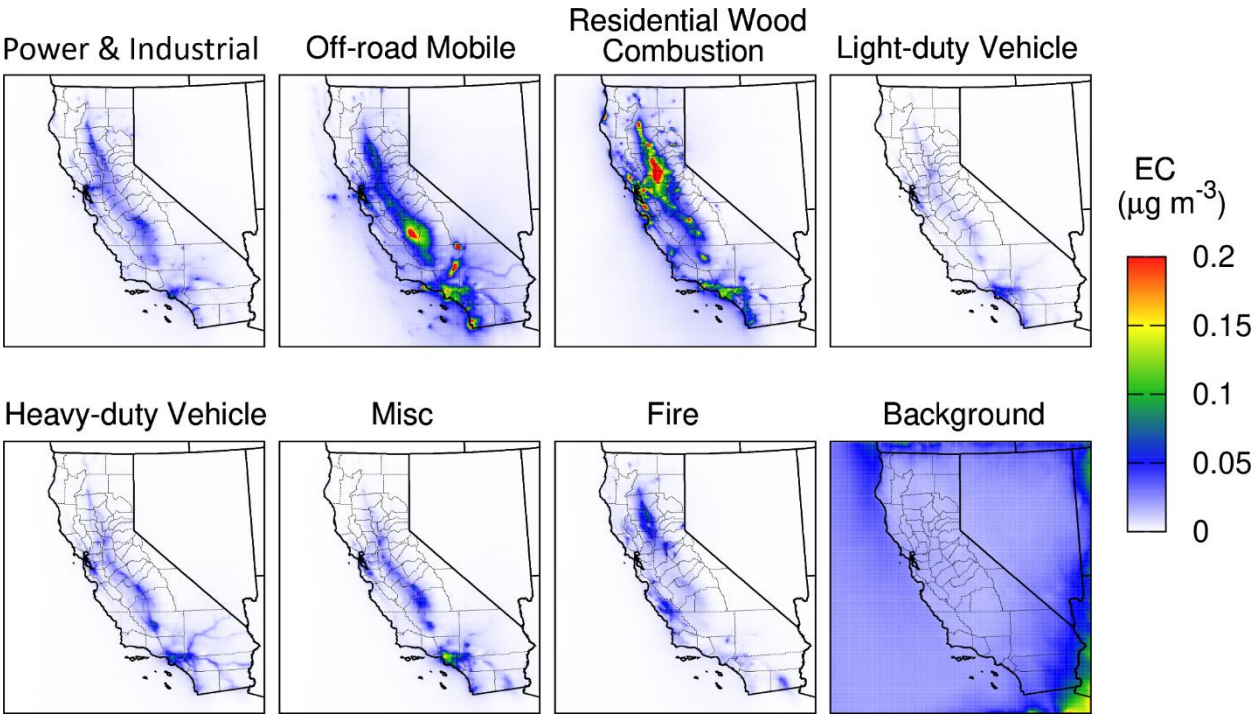

Figure 2 Spatial distribution of CMAQ modeled annual EC concentrations attributable to emission sectors and background based on the prior emission inventory.

The modified CMAQ was applied with the SAPRC07tic gas-phase photochemical mechanism[38] and the aerosol module version 6 (AERO6) to simulate atmospheric concentrations of particulate and gas-phase species in 2019. EC and its source-specific tracers are treated as chemically inert, with aging represented through size-dependent dry deposition and wet scavenging. Our domain consists of 277×289 grids at 4km × 4km horizontal resolution, covering the entire state of California (Figure 1). The vertical structure includes 30 stretching layers, with the first layer height of ~30 m above ground and the model top set at approximately 100 hPa. Initial and boundary conditions for the domain were generated using the Mozart2CAMx preprocessor[39], which converts chemical data from Community Atmosphere Model with Chemistry (CAM-CHEM) outputs[40] into the format compatible with CMAQ. The first 5 days of the simulation results were treated as spin-up and excluded from the analysis.

Meteorological inputs were generated using Weather Research & Forecasting (WRF) Model v4.6. Initial and boundary conditions were provided by the High-Resolution Rapid Refresh (HRRR) v4 dataset[41], which is in hourly and 3-km horizontal resolution. The land use/land cover and topographical data are based on the 30s resolution default WRF input dataset. Four-dimensional data assimilation (FDDA) via reanalysis nudging was enabled to improve the agreement between predicted and observed meteorological parameters. WRF was run in 5-day segments, and each

segment included a 12-hour spin-up period, which was discarded. The raw WRF outputs were subsequently processed using the Meteorology-Chemistry Interface Processor (MCIP) v5.5 to generate the gridded CMAQ-ready input files. As summarized in Table S3, the meteorological performance statistics in this study are comparable to previous high-resolution modeling studies and are consistent with established benchmarks.[42–45]

Log-space Bayesian inversion

We employ a Bayesian inverse modeling approach to optimize EC emissions by integrating surface observations with prior information from the bottom-up inventory. The optimization is performed in log-space, which more accurately characterizes the multiplicative error structure and log-normal distribution of atmospheric data.[46] This log-transformation ensures the physical positivity of the solution by preventing the retrieval of non-physical negative emissions, which is a common limitation in linear inversion schemes.[47] Specifically, we assume that sector-specific adjustment factors are invariant in both time and space across the domain.

The relationship between emissions and modeled concentrations is represented by a linear function, $\boldsymbol{y}_{\mathbf{mod}} = \boldsymbol{K}\boldsymbol{\lambda}$, where $\boldsymbol{y}_{\mathbf{mod}}$ is the $n \times 1$ vector of modeled daily concentrations across all sites. The source-receptor matrix $\boldsymbol{K}$ $(n \times m)$ characterizes the sensitivity of the n concentrations to the m emission sectors, essentially storing the contribution of each sector to each specific observation, as determined by the source-tagged CMAQ simulation. $\boldsymbol{\lambda}$ is the $m \times 1$ vector of source-specific scaling factors. To optimize the emissions, we minimize a cost function $J(\boldsymbol{L})$ that reconciles the discrepancies between modeled and observed data, as Eq. (1):

$$J(\boldsymbol{L}) = \left(\boldsymbol{L} - \boldsymbol{L}_{\mathbf{prior}}\right)^{T} \boldsymbol{S}_{\mathbf{prior}}^{-1} \left(\boldsymbol{L} - \boldsymbol{L}_{\mathbf{prior}}\right) + \left(\ln(\boldsymbol{y}_{\mathbf{obs}}) - \ln(\boldsymbol{K}e^{\boldsymbol{L}})\right)^{T} \boldsymbol{S}_{\boldsymbol{e}}^{-1} \left(\ln(\boldsymbol{y}_{\mathbf{obs}}) - \ln(\boldsymbol{K}e^{\boldsymbol{L}})\right) \quad (1)$$

where, $\boldsymbol{L}$ (m×1) is the state vector of log-transformed scaling factors between the posterior emissions ($\boldsymbol{E}_{\mathbf{post}}$) and prior emissions ($\boldsymbol{E}_{\mathbf{prior}}$), $\boldsymbol{L} = \ln(\boldsymbol{\lambda}) = \ln\left(\frac{\boldsymbol{E}_{\mathbf{post}}}{\boldsymbol{E}_{\mathbf{prior}}}\right)$. $\boldsymbol{L}_{\mathbf{prior}}$ $(= \mathbf{0})$ is the log transformed prior scaling factor of 1, to represent the baseline inventory. The observational error covariance matrix $(\boldsymbol{S}_{\boldsymbol{e}})$ accounts for both site-specific residual variance (σ_k^2) and temporal correlation between measurements at the same site *k*. The residual variance (σ_k^2), defined as the variance of differences between the log-transformed model predictions and observations at site *k*, represents the combined uncertainty from measurement noise, model transport errors, and representativeness errors. This term quantifies the "mismatch" between observation points and grid-averaged model predictions that cannot be explained by emission scaling alone. The temporal correlation for measurements *i* and *j* at the same site is estimated as $\rho_{ij} = \exp\left(-\frac{|t_i - t_j|}{\tau}\right)$, where $t_i - t_j$ represents the time difference in days between two measurements *i* and *j*. The decay

constant τ is set to 5 days, consistent with the typical atmospheric lifetime of EC.[48,49] The elements of $(\boldsymbol{S_e})$ are represented as Eq. (2):

$$S_e(i,j) = \begin{cases} \sigma_k^2, & t_i = t_j, i \text{ and } j \text{ are measured at the same site } k \\ \rho_{ij}\sigma_k^2, & t_i \neq t_j, i \text{ and } j \text{ are measured at the same site } k \\ 0, & i \text{ and } j \text{ are measured at different sites} \end{cases} \quad (2)$$

The prior error covariance matrix $\left(\boldsymbol{S}_{\mathbf{prior}}\right)$ is a diagonal matrix of sector-specific variances of the log-scale factors $\boldsymbol{L}$. Since the inversion is performed in log-space, the prior variance for each sector is defined as $\sigma^2 = \left[\ln\left(1 + \frac{\sigma_\lambda}{\lambda}\right)\right]^2$, where σ_λ denotes the standard deviation of the EC/Pri-$PM_{2.5}$ ratios for each emission sector. This $\boldsymbol{S_{prior}}$ explicitly focuses on the speciation and emission factor uncertainties that are the primary drivers of total mass in the sector-scaling approach. The sector-specific values of $\left(\frac{\sigma_\lambda}{\lambda}\right)$ are summarized in Table S2.

The Maximum a Posteriori (MAP) estimate is derived by minimizing the cost function $J(\boldsymbol{L})$ in Eq. (1) to find the most probable state of the log-scaling factors given the available observations. The minimization is performed using the gradient of the cost function, which is expressed in Eq. (3):

$$\nabla_{\boldsymbol{L}} J(\boldsymbol{L}) = -2\boldsymbol{J}_{\boldsymbol{mat}}^T(\boldsymbol{L})\boldsymbol{S}_{\boldsymbol{e}}^{-1}(\ln(\boldsymbol{y}_{\mathbf{obs}}) - \ln(\boldsymbol{K}e^{\boldsymbol{L}})) + 2\boldsymbol{S}_{\mathbf{prior}}^{-1}\left(\boldsymbol{L} - \boldsymbol{L}_{\mathbf{prior}}\right) \quad (3)$$

where, $\boldsymbol{J_{mat}}(\boldsymbol{L})$ is the Jacobian matrix, which defines the sensitivity of the log-modeled concentrations to the log-scaling factors, as Eq. (4):

$$\boldsymbol{J_{mat}}(\boldsymbol{L}) = \frac{\partial \ln(\boldsymbol{K}e^{\boldsymbol{L}})}{\partial \boldsymbol{L}} \quad (4)$$

The obtained state vector $\boldsymbol{L}$ contains the optimized log-scaling factors for each emission sector. Once the optimized emissions (defined as $\boldsymbol{E}_{\mathbf{post}} = \boldsymbol{E}_{\mathbf{prior}} \cdot e^{\boldsymbol{L}}$) are obtained, the posterior covariance matrix for $\left(\boldsymbol{S}_{\mathbf{post}}\right)$ is calculated to quantify the uncertainty of the log-space optimized emissions, in Eq. (5):

$$\boldsymbol{S}_{\mathbf{post}} = \left(\boldsymbol{J}_{\boldsymbol{mat}}^T(\boldsymbol{L})\boldsymbol{S}_{\boldsymbol{e}}^{-1}\boldsymbol{J_{mat}}(\boldsymbol{L}) + \boldsymbol{S}_{\mathbf{prior}}^{-1}\right)^{-1} \quad (5)$$

This matrix represents the updated uncertainty in the log-transformed scaling factors. It reflects the degree of reduction from the prior uncertainty due to the information gain provided by the observational data during the inversion process.

Results and Discussions

Optimized sector-specific scaling factors

By comparing model results against EPA's AQS daily EC measurements, the CMAQ model performance for total $PM_{2.5}$ consistently meet the PM performance goals and criteria suggested by Boylan and Russell [50], as shown in Table S4. This indicates that the model reasonably captures the overall mass of fine particles and the underlying transport processes. However, the modeled prior EC concentrations in the domain exhibits a significant negative bias, with a Mean Fractional Bias ($MFB = \frac{1}{N}\sum_{i=1}^{N}\left(2\frac{c_{m,i}-c_{o,i}}{c_{m,i}+c_{o,i}}\right)$) of -0.48, when compared with the daily observations from all 34 monitoring sites located in Figure 1a. This systematic negative bias indicates a significant underestimation in California's EC emission inventory. While our findings reflect the region's distinct 2019 regulatory and emission context, this discrepancy is directionally consistent with the previous top-down analyses.[19–21]

Following the log-space Bayesian inversion, model performance based on posterior emissions for EC shows a remarkable improvement, as Figure S2. The MFB is significantly reduced from -0.48 to -0.25, while the regression slope increases from 0.59 to 0.71. This improvement indicates that the inversion framework successfully mitigates systematic underestimation of EC emissions. The Pearson correlation coefficient (R) remains constant of 0.70. As presented in Figure 1b, the modeled posterior EC concentrations demonstrates better agreement with the observations compared to the prior simulation (Figure 1a).

The log-space Bayesian inversion derives source-specific scaling factors (λ) (Table S5) that are used to adjust the discrepancies in the prior emission inventory. The largest adjustment occurred in the emission of power & industrial sector, which requires an increase by a factor of 2.63 with 95% confidence interval [2.15–3.21], indicating that baseline emissions for this sector were underestimated by more than a factor of 2. Off-road mobile source followed with a $\lambda = 1.72$ [1.51–1.96]. Both light- and heavy-duty vehicles show similar upward adjustments of approximately 30% ($\lambda \approx 1.30$). This is largely attributed to the highly correlated spatial distributions along major transportation corridors. Due to large uncertainties in the temporal allocation of the prescribed burning and structural fires that is unresolvable by the annual scaling factor, the fire sector was fixed and not subject to scaling ($\lambda = 1.00$). However, we conducted sensitivity tests by arbitrarily scaling prior fire emissions by factors of 0.5 and 2.0. The results (Figure S3) demonstrate that the optimized λ values for other sectors remained relatively robust. Background EC was also held constant to ensure the inversion focused specifically on reconciling local anthropogenic discrepancies rather than potentially over-adjusting for long-range transport. This is supported by the fact that background contributions remain below 10% in regions where the monitoring sites are densely distributed (Figure S4), and the persistent posterior MFB of -0.25 indicates that the inversion leaves residual mismatch as error rather than forcing an artificial match through the optimized sectors.

Each diagonal element of $\boldsymbol{S_{post}}$ is the posterior variance of a given sector's log-scaling factor, and its square root gives the posterior uncertainty σ. Post-inversion, posterior uncertainties are significantly reduced across several sectors (Table S5), particularly for residential wood combustion (σ decreased from 0.33 to 0.06) and off-road mobile (0.15 to 0.07), indicating that the AQS observation network provides strong constraints for these specific sources.

The off-diagonal elements of $\boldsymbol{S_{post}}$ represent posterior covariances between sectoral scaling factors, arising from shared observational constraints through the Jacobian matrix ($\boldsymbol{J_{mat}(L)}$). The posterior correlation matrix $r_{ij} = \frac{S_{post,ij}}{\sqrt{S_{post,ii}}\cdot\sqrt{S_{post,jj}}}$ quantifies the degree to which sector pairs are independently resolved by the monitoring network. The posterior correlation matrix of ln(λ) (Figure S5) shows weak-to-moderate negative correlations among all sectors, indicating minor compensating adjustment. The strongest correlation occurs between power & industrial and off-road mobile sources (-0.31), reflecting the extent to which these two sources are co-located in California, such as ports in Los Angeles and concentrated agriculture and industrial activities in the San Joaquin Valley. Similarly, off-road mobile and light-duty vehicles show moderate correlation (-0.28) due to shared receptor footprints. Conversely, light-duty and heavy-duty vehicles show a relatively weak correlation (-0.15) despite sharing freight corridors networks. Residential wood combustion shows near-zero correlations with all other sectors ($|r| < 0.10$), reflecting its distinct seasonal and spatial signature. Overall, the results indicate that all sectors retain meaningful independent constraint from the observational network, and the sectoral attribution is not undermined by posterior co-dependence.

Posterior sectoral emissions

The inversion results, summarized in Table 1, reveal a substantial increase in total EC emissions for California in 2019, rising from a prior mean estimate of 8.58 Gg yr^{-1} to a posterior mean estimate of 12.78 Gg yr^{-1}. This represents a 33% underestimation in the current California EC bottom-up inventory. The most significant discrepancies are found in the power & industrial sector, where the emissions are increased from 1.02 [0.60–1.71] Gg yr^{-1} to 2.67 [2.18–3.27] Gg yr^{-1}, and the off-road mobile sector, which increased from 3.10 [2.32–4.16] Gg yr^{-1} to 5.33 [4.69–6.07] Gg yr^{-1}. These two categories alone account for the majority of the "missing" EC emissions reconciled by the top-down approach.

Table 1 California 2019 EC sectoral emission budgets (Prior vs. Posterior) (Gg yr^{-1})

Sector	Prior Emissions	Posterior Emissions
Power & Industrial	1.02 [0.60–1.71] [a]	2.67 [2.18–3.27]

Off-road Mobile	3.10 [2.32–4.16]	5.33 [4.69–6.07]
Residential wood Combustion	2.51 [1.31–4.79]	2.39 [2.12–2.69]
Light-duty Vehicle	0.46 [0.28–0.76]	0.60 [0.38–0.94]
Heavy-duty Vehicle	0.69 [0.52–0.93]	0.91 [0.71–1.16]
Miscellaneous	0.80 [0.46–1.39]	0.88 [0.62–1.23]
Total	**8.58 [5.49–13.75]**	**12.78 [10.71–15.37]**

[a] Values represent the mean with 95% confidence interval derived from the standard deviation (σ) of log-space scaling factor ($[E \cdot e^{-1.96\times\sigma} - E \cdot e^{+1.96\times\sigma}]$) attributed to prior and posterior uncertainties in Bayesian inversion framework.

The emissions from residential wood combustion are well-captured in the prior inventory, with a slight decrease from 2.51 [1.31–4.79] Gg yr^{-1} to 2.39 [2.12–2.69] Gg yr^{-1}. Since winter temperature in California 2019 align with the long-term average, our inverted woodsmoke emission estimates are likely representative of typical seasonal conditions. As discussed previously, EC emissions from both light- and heavy-duty vehicles show moderate increases of approximately 30%. The spatial distribution of posterior EC emissions for each sector is shown in Figure S6. Notably, the 95% confidence intervals narrowed significantly across all sectors through Bayesian inversion. The total emission uncertainty range has been tightened from [5.49–13.75] Gg yr^{-1} to [10.71–15.37] Gg yr^{-1}.

Figure S7 illustrates the comparative analysis of California's EC bottom-up emission estimates, highlighting the sectoral changes between the 2013 CARB baseline and our 2019 bottom-up (prior) estimates. Both estimates represent traditional bottom-up inventories, derived by applying CARB's chemical speciation profiles to source-specific $PM_{2.5}$ emission estimates. Comparing the bottom-up inventories from 2013 to 2019 reveals a 25% decline in total estimated EC emissions, falling from 11.50 Gg yr^{-1} to 8.58 Gg yr^{-1}. This decrease is primarily driven by the reduction in heavy-duty vehicle sector, which dropped from 2.19 Gg yr-1 (19% of 2013 total) to 0.69 Gg yr^{-1} (8% of the 2019 prior), likely following the widespread implementation of advanced emission control technologies.[51–53] In contrast, residential wood combustion emerged as a more predominant source in the 2019 prior inventory, representing 29% of total EC emissions compared to a 16% share observed in 2013.

While these bottom-up inventories capture regulatory-driven declines, the comparison of sectoral contribution shares between our 2019 prior (bottom-up) and posterior (top-down) estimates reveals a significant structural reallocation of emission sources, as Figure 3. The posterior results indicate that the off-road mobile sector is even more dominant than prior estimation, with its share increasing from 36% to 42%. The most dramatic shift occurs in the power

& industrial sector, which nearly doubles its relative contribution from 12% in the prior to 21% in the posterior. This underestimation in the prior was also identified by Rönkkö et al.[16] and the adjustment is supported by the strong observational constraint with uncertainty reduced from 0.27 to 0.10. In contrast, the relative importance of residential wood combustion is notably lower in the posterior than in the prior estimates, falling from 29% to 19%, and only slightly higher than its contribution share (16%) in the 2013 inventory. This shift may in part be attributed to the impact of the California Woodsmoke Reduction Program implemented since 2016, which offers financial incentives to homeowners to replace their woodstoves or fireplaces with cleaner and more efficient home heating devices. Minor relative decreases were also observed in the heavy-duty (8% to 7%), light-duty vehicles (6% to 4%), and miscellaneous (9% to 7%) sectors.

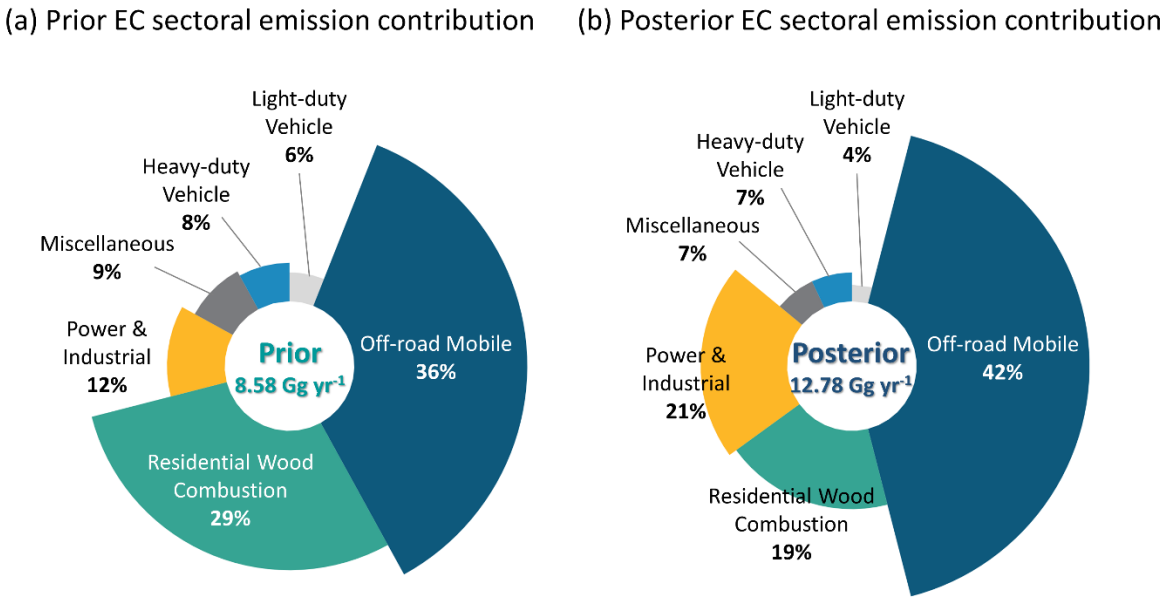

Figure 3. Statewide EC sector emission contributions in 2019 for California. (a) Prior sectoral emission composition estimated based on CARB inventory; (b) Posterior sectoral emission composition derived from Bayesian inversion in this study.

Sectoral contributions to population-weighted EC exposure concentration

To assess the public health implications of our posterior emission inventory, we calculated the population-weighted EC exposure concentration across California. This metric was obtained by overlaying the EC concentrations for each sector with high-resolution population density data from the US Census Bureau's TIGER/Line 2020 California shapefiles.[54] The sector-specific uncertainties (95% CI) in posterior emissions are explicitly propagated into the population-

weighted exposure estimates. The posterior statewide population-weighted average EC concentration for 2019 was determined to be 0.49 [0.41-0.59] μg m^{-3}, increased from 0.38 [0.24-0.60] μg m^{-3} based on prior estimates. This approach provides a more health-relevant assessment than mass emissions alone, as it accounts for the spatial proximity between emission sources and densely populated areas.

While the statewide EC emission budget is dominated by off-road mobile and power & industrial activities, the exposure analysis reveals disproportionate health burdens from residential and nearby off-road mobile sources, as consistently shown in both the prior (Figure S8) and posterior results (Figure 4a). Figure 4a indicates while off-road is the leading exposure source, its contribution share decreases significantly from 42% in emissions to 31% in exposure. Similarly, the power & industrial sector's contribution is reduced from 21% in emissions to 14% of total exposure. In contrast, while residential wood combustion accounts for 19% of the total EC emissions, it is responsible for a much higher 26% of the total population exposure. This shift is attributed to the fact that wood smoke is primarily emitted at ground level within residential neighborhoods, resulting in higher intake fractions compared to remote industrial stacks.

Compared with exposure estimates based on the prior emissions inventory, the top-down posterior results indicate substantially higher exposure risks to power & industrial sources, with their shares of total exposure roughly doubling from 7% to 14%. On the other hand, off-road mobile sources remain the largest driver of both emissions and exposure in prior and posterior results, verifying their role as the most significant contributor to California EC-related health risks in 2019. Collectively, light- (7%) and heavy-duty vehicles (9%) account for 16% of the statewide EC exposure.

Beyond the statewide patterns, the regional analysis in Figure 4b illustrates how these top-down estimated posterior emissions translate into local health risks across California's air basins. While the statewide population-weighted average EC concentration is 0.49 [0.41-0.59] μg m^{-3}, the South Coast air district has a much higher exposure level of 0.58 [0.48-0.72] μg m^{-3}, predominantly driven by a high concentration of off-road mobile sources from nearby ports (33%). In the San Francisco Bay Area air district, EC exposure (0.43 [0.37-0.51] μg m^{-3}) is similarly influenced by the proximity of residents to ground-level sources, with residential wood combustion accounting for a substantial 36% of the total exposure. The most dramatic shift between emissions and human intake is observed in the San Joaquin Valley (average exposure 0.47 [0.40-0.57] μg m^{-3}). Although off-road mobile sources account for more than half of total emissions in this district, their contribution to population exposure is much lower (about 30%). This reduction reflects the fact that many off-road emissions originate from rural agricultural activities located farther away from major population centers in the valley. Conversely, residential wood combustion represents only 7% in the regional emissions, but accounts for a much higher 26% of exposure. This large increase in relative impact is attributed to the fact that woodsmoke is emitted at ground level within residential areas and is frequently trapped by the valley's unique topography and stagnant winter air.[55,56] The spatial distributions of sectoral EC exposure are presented in Figure S9.

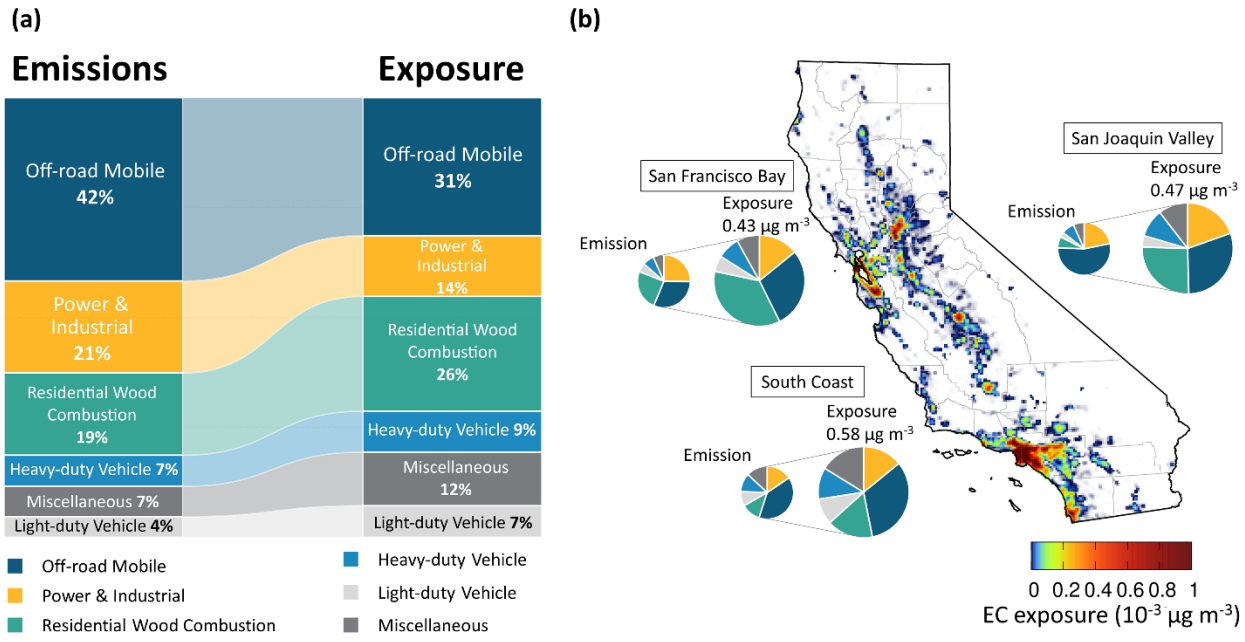

Figure 4. Analysis of EC exposure and sectoral contributions based on posterior results in California. (a) Sectoral contributions to statewide emissions and population-weighted EC exposure; (b) Spatial distribution of annual mean EC exposure. The inset pie charts compare the source contributions for EC emission and exposure in three air districts: San Francisco Bay, South Coast, and San Joaquin Valley.

Implications on EC speciation profiles

Past top-down assessments[19–21] and this study suggest that EC emission inventories are systematically underestimated. This discrepancy is likely due to the methodology used to derive EC emissions as a mass fraction of the total primary $PM_{2.5}$. While bottom-up $PM_{2.5}$ inventories are generally considered more reliable because of rigorous regulatory reporting and monitoring, the EC mass fractions (f_{EC}, or speciation profiles) are often outdated or poorly constrained. Since sectoral EC emissions are calculated by multiplying the $PM_{2.5}$ emission rate by the uncertain f_{EC} values, errors in f_{EC} propagate into the final EC emission estimates. Refining these f_{EC} values through inverse modeling is therefore essential to addressing the underestimation of EC in current inventories.

To calculate the prior and posterior f_{EC} for each source sector, we utilized the total sectoral pri-$PM_{2.5}$ emission rates and the corresponding EC emissions before and after our Bayesian inversion. The modeled pri-$PM_{2.5}$ concentrations were validated using the AQS surface measurements, as described in Section S1 of supplemental information. As shown in Table 2, the prior sectoral aggregated f_{EC} was determined by dividing the initial bottom-up EC emission rates (Prior Emissions in Table 1) by total $PM_{2.5}$ emissions for each sector. The posterior f_{EC} was similarly derived by dividing the optimized EC emission rates (Posterior Emissions in Table 1) by

the same $PM_{2.5}$ inventory. The uncertainty ranges presented in the brackets represent the 95% confidence intervals derived from the Bayesian prior and posterior distributions.

A review of bottom-up inventory literatures is shown in Table 2, which includes reported speciation profiles of both BC and EC. Despite different measurement methods of BC and EC,[57,58] most literatures have treated EC measurements as interchangeable proxies for BC.[59,60] Reported f_{EC} values exhibit substantial variability that largely arises from inconsistencies in source classification and reporting methodologies. Despite these wide ranges, our posterior f_{EC} estimates generally align with previously reported values. For the power & industrial sector, the inversion adjusted f_{EC} to 12.6% [7.5% - 21.1%] from a prior of 4.8% [2.8 – 8.0%], positioning the posterior f_{EC} close to the upper bound reported by Chow et al.[61] This sector aggregates a highly diverse array of sources, including power generation, petroleum refining, and specialized industrial processes, with highly heterogeneous and often poorly characterized EC emission factors, which are likely relied on limited source testing data. Posterior f_{EC} values for residential wood combustion (16.6%) and power & industrial (12.6%) remained stable and within the broad uncertainties of Klimont et al.[26] and Chow et al.[61] The f_{EC} for the miscellaneous sector remained lower than the literature benchmarks, primarily because of the highly complex and diverse sources aggregated within this category.

The off-road mobile sector exhibited substantial improvement, with the posterior f_{EC} increased to 53.0% [39.5–71.0%] from a prior estimate of 30.8%. The result aligns more closely with the diesel engine profile of 66% reported by Bond et al.[59] and the 44.0% reported by Klimont et al.[26], suggesting the prior f_{EC} significantly underestimates the EC emissions for off-road diesel equipment. For the heavy-duty vehicle sector, the inversion resulted in a posterior f_{EC} of 43.8% [32.7–58.6%]. This value is highly consistent with the frequently reported ranges of 32–74% from Chow et al.[61,62] and moved closer to the diesel engine profile of Bond et al.[59] In comparison, Klimont et al.[26] reported a combined on-road f_{EC} of 46.1%, which does not provide a separate split for light- and heavy-duty vehicles. Our heavy-duty vehicle f_{EC} remains remarkably similar to their aggregated on-road transportation estimate. The posterior f_{EC} for light-duty vehicle increased to 19.8% [12.0–32.7%], demonstrating high consistency with the 22.0% mean value reported by Chow et al.[62] and the gasoline engine profile (34.0%) of Bond et al.[59]

To further validate our on-road results, we expanded the comparison of the posterior f_{EC} with literature that accounts for evolving vehicle technologies and emission standards, as Table S6. Our posterior light-duty vehicle f_{EC} (19.8%) aligns well with the measurements of light-duty gasoline vehicles, such as the 20.0% lower bound from May et al.[63] In Sonntag et al.'s study,[64] the f_{EC} values were measured of 14.0±2.7% during running and 44.4±4.3% for start. Applying the $PM_{2.5}$ emission weighting factors from the CARB on-road inventory (85% for running and 15% for start), the weighted average of f_{EC} is 18.7%, which is remarkably consistent with our posterior results.

The particulate emissions from heavy-duty vehicles have undergone a significant evolution since 2007, primarily driven by the mandatory implementation of diesel particulate filters (DPFs)

and selective catalytic reduction (SCR) systems. These technologies have fundamentally altered the chemical composition of diesel exhaust by reducing the total mass of primary $PM_{2.5}$ and changing the relative proportion of EC. While pre-2007 engines typically exhibit high f_{EC}, such as 51.9% - 61.4% reported by Ban-Weiss et al.,[65] modern DPF-equipped engines can achieve f_{EC} as low as 13% based on Khalek et al.[66,67] Our posterior f_{EC} of 43.8% for heavy-duty vehicles likely reflects a "transition fleet" in California during 2019, representing a composite of controlled newer trucks and older, high-emitting vehicles that remain in operation.

Table 2. Comparison of sector-specific EC mass fractions (f_{EC}, unit: %) in emissions.

Sector	**This study Prior** [a]	**This study Posterior**	**Bond et al. (2004)**	**Chow et al. (2009)** [c]	**Chow et al. (2011)** [d]	**Klimont et al. (2017)** [e]
Power & Industrial	4.8 [2.8–8.0] [b]	12.6 [7.5–21.1]	-	-	0.46–13.6	7.7
Off-road Mobile	30.8 [23.0–41.3]	53.0 [39.5–71.0]	66.0	41.0 [21.0–61.0]	-	44.0
Residential Wood Combustion	17.4 [9.1–33.3]	16.6 [8.7–31.8]	-	9.6 [0.0–21.8]	4.2–33.0	19.0
Light-duty Vehicle	15.2 [9.2–25.1]	19.8 [12.0–32.7]	34.0	22.0 [8.0–36.0]	5.9–37.0	46.1
Heavy-duty Vehicle	33.4 [24.9–44.8]	43.8 [32.7–58.6]	66.0	51.0 [32.0–70.0]	33.0–74.0	
Miscellaneous	1.3 [0.8–2.4]	1.5 [0.8–2.6]	-	-	3.6–26.0	14.9

[a] The f_{EC} values for this study were calculated using the prior and posterior EC emissions derived in this study. The pri-$PM_{2.5}$ emissions are assumed to be a reliable baseline for these calculations.
[b] The values in brackets for this study represent the 95% confidence interval.
[c] Reported values represent the mean, while ranges within brackets indicate the uncertainties based on ±1 standard deviation.
[d] The ranges provided for each sector reflect the variability of f_{EC} across related source categories within that specific sector.
[e] The f_{EC} values were derived from the 2010 sectoral emission inventory. Due to the lack of independent sub-sector data in the source inventory, light- and heavy-duty vehicles were merged for this comparison.

While our inversion framework enables sector-level posterior inference statewide, constraining localized emissions remains challenging—particularly in areas where local biases differ substantially from other regions and are not captured by the sparsely distributed AQS monitors. In

future research, incorporating dense low-cost sensor networks with expanded spatial coverage could help mitigate these limitations, enabling emissions to be estimated at hyperlocal scales.[68]

On the other hand, the inferred posterior emissions are sensitive to the EC measurement protocols. This study employs IMPROVE-based EC as observational constraints; utilizing alternative monitoring protocols could impose different constraints and thus produce different posterior emission estimates. While interlaboratory comparisons show strong agreement for the total carbon (TC) with well-calibrated instruments, the organic carbon (OC) and EC splits remain protocol-dependent. [69–71] Specifically, the IMPROVE protocol consistently yields lower OC/EC ratios and higher EC mass fractions compared with NIST-EPA and NIOSH protocols. [72] This discrepancy is primarily driven by the lower peak temperature in the inert helium phase of the IMPROVE protocol, which results in less OC evolving before the oxidizing phase. The formation of pyrolytic carbon (Pyrol C or OP) during thermal analysis can artificially increase EC concentrations if not accurately corrected. Although optical monitoring is employed to distinguish original EC from Pyrol C, the exact "split point" is difficult to determine and varies significantly by ambient sampling composition, such as organic chemicals, graphite, diesel exhaust, and wood smoke. [73,74] Additional sensitivity analyses evaluating potential systematic biases of observations and prior covariance in our inversion framework are discussed in Section S2 of the Supplementary Information. These uncertainties suggest that future inverse modeling efforts should incorporate various observations, including BC measurements from aethalometer-based optical absorption, to achieve more robust, source-resolved emission estimates.

Supporting Information

Additional figures include: Comparison of observed daily EC concentrations measured by the CSN and IMPROVE network (Figure S1); Comparison of prior and posterior CMAQ model performance (Figure S2); Sensitivity analysis of optimized scaling factor to fire emissions (Figure S3); Spatial distribution of posterior EC emissions (Figure S4); Comparison of sectoral emissions from CARB 2013 inventory and 2019 bottom-up inventory (Figure S5); Sectoral contributions to statewide emission and population-weighted EC exposure based on prior estimates (Figure S6); Source-specific spatial distribution of EC exposure concentrations (Figure S7). Additional tables include: EC measurement protocols in US EPS's Air Quality System (Tables S1); Summary of annual prior emissions for pri-$PM_{2.5}$ and EC (Table S2); Monthly meteorological performance statistics (Table S3); Model performance of total $PM_{2.5}$ concentrations (Table S4); Prior and posterior scaling factors and corresponding uncertainties in log-space (Table S5); Comparison of on-road EC mass fraction (%) with literatures (Table S6). Detailed information for: Model performance of primary $PM_{2.5}$ (Section S1); Sensitivity analysis of inverse modeling (Section S2).

Acknowledgement

The authors acknowledge the U.S. DOE Office of Clean Energy Demonstrations for funding this research in Fiscal Year 2025. The work was conducted in-part by researchers at Lawrence

Berkeley National Laboratory under Contract No. DE-AC02-05CH11231 to the U.S. DOE. Model simulations were conducted on the Lawrencium high performance computing cluster at Lawrence Berkeley National Laboratory. The views expressed in the article do not necessarily represent the views of the DOE or the U.S. Government. The U.S. Government retains a nonexclusive, paid-up, irrevocable, worldwide license to publish or reproduce the published form of this work, or allow others to do so, for U.S. Government purposes.to do so, for U.S. Government purposes.

References

(1) Allen, G. A.; Lawrence, J.; Koutrakis, P. Field Validation of a Semi-Continuous Method for Aerosol Black Carbon (Aethalometer) and Temporal Patterns of Summertime Hourly Black Carbon Measurements in Southwestern PA. *Atmospheric Environment* **1999**, *33* (5), 817–823. https://doi.org/10.1016/S1352-2310(98)00142-3.

(2) Zhang, Z.; Cheng, Y.; Liang, L.; Liu, J.; Zhang, Z.; Cheng, Y.; Liang, L.; Liu, J. The Measurement of Atmospheric Black Carbon: A Review. *Toxics* **2023**, *11* (12). https://doi.org/10.3390/toxics11120975.

(3) Liu, F.; Yon, J.; Fuentes, A.; Lobo, P.; Smallwood, G. J.; Corbin, J. C. Review of Recent Literature on the Light Absorption Properties of Black Carbon: Refractive Index, Mass Absorption Cross Section, and Absorption Function. *Aerosol Science and Technology* **2020**, *54* (1), 33–51. https://doi.org/10.1080/02786826.2019.1676878.

(4) Zhang, Y.; Zhang, Q.; Cheng, Y.; Su, H.; Li, H.; Li, M.; Zhang, X.; Ding, A.; He, K. Amplification of Light Absorption of Black Carbon Associated with Air Pollution. *Atmospheric Chemistry and Physics* **2018**, *18* (13), 9879–9896. https://doi.org/10.5194/acp-18-9879-2018.

(5) Jacobson, M. Z. Strong Radiative Heating Due to the Mixing State of Black Carbon in Atmospheric Aerosols. *Nature* **2001**, *409* (6821), 695–697. https://doi.org/10.1038/35055518.

(6) Menon, S.; Hansen, J.; Nazarenko, L.; Luo, Y. Climate Effects of Black Carbon Aerosols in China and India. *Science* **2002**, *297* (5590), 2250–2253. https://doi.org/10.1126/science.1075159.

(7) Ramanathan, V.; Carmichael, G. Global and Regional Climate Changes Due to Black Carbon. *Nature Geosci* **2008**, *1* (4), 221–227. https://doi.org/10.1038/ngeo156.

(8) Gustafsson, Ö.; Ramanathan, V. Convergence on Climate Warming by Black Carbon Aerosols. *Proceedings of the National Academy of Sciences* **2016**, *113* (16), 4243–4245. https://doi.org/10.1073/pnas.1603570113.

(9) Peng, R. D.; Bell, M. L.; Geyh, A. S.; McDermott, A.; Zeger, S. L.; Samet, J. M.; Dominici, F. Emergency Admissions for Cardiovascular and Respiratory Diseases and the Chemical Composition of Fine Particle Air Pollution. *Environ Health Perspect* **2009**, *117* (6), 957–963. https://doi.org/10.1289/ehp.0800185.

(10) Janssen, N. A. H.; Hoek, G.; Simic-Lawson, M.; Fischer, P.; van Bree, L.; ten Brink, H.; Keuken, M.; Atkinson, R. W.; Anderson, H. R.; Brunekreef, B.; Cassee, F. R. Black Carbon as an Additional Indicator of the Adverse Health Effects of Airborne Particles Compared with PM10 and PM2.5. *Environ Health Perspect* **2011**, *119* (12), 1691–1699. https://doi.org/10.1289/ehp.1003369.

(11) Anenberg, S. C.; Talgo, K.; Arunachalam, S.; Dolwick, P.; Jang, C.; West, J. J. Impacts of Global, Regional, and Sectoral Black Carbon Emission Reductions on Surface Air Quality and Human Mortality. *Atmospheric Chemistry and Physics* **2011**, *11* (14), 7253–7267. https://doi.org/10.5194/acp-11-7253-2011.

(12) Ostro, B. D.; Feng, W.-Y.; Broadwin, R.; Malig, B. J.; Green, R. S.; Lipsett, M. J. The Impact of Components of Fine Particulate Matter on Cardiovascular Mortality in Susceptible Subpopulations. *Occup Environ Med* **2008**, *65* (11), 750–756. https://doi.org/10.1136/oem.2007.036673.

(13) Bell, M. L.; Ebisu, K.; Peng, R. D.; Samet, J. M.; Dominici, F. Hospital Admissions and Chemical Composition of Fine Particle Air Pollution. *Am J Respir Crit Care Med* **2009**, *179* (12), 1115–1120. https://doi.org/10.1164/rccm.200808-1240OC.

(14) Ostro, B.; Feng, W.-Y.; Broadwin, R.; Green, S.; Lipsett, M. The Effects of Components of Fine Particulate Air Pollution on Mortality in California: Results from CALFINE. *Environ Health Perspect* **2007**, *115* (1), 13–19. https://doi.org/10.1289/ehp.9281.

(15) Ban-Weiss, G. A.; Lunden, M. M.; Kirchstetter, T. W.; Harley, R. A. Measurement of Black Carbon and Particle Number Emission Factors from Individual Heavy-Duty Trucks. *Environ Sci Technol* **2009**, *43* (5), 1419–1424. https://doi.org/10.1021/es8021039.

(16) Rönkkö, T.; Saarikoski, S.; Kuittinen, N.; Karjalainen, P.; Keskinen, H.; Järvinen, A.; Mylläri, F.; Aakko-Saksa, P.; Timonen, H. Review of Black Carbon Emission Factors from Different Anthropogenic Sources. *Environ. Res. Lett.* **2023**, *18* (3), 033004. https://doi.org/10.1088/1748-9326/acbb1b.

(17) Jacob, D. Inverse Modeling Techniques. In *Observing Systems for Atmospheric Composition: Satellite, Aircraft, Sensor Web and Ground-Based Observational Methods and Strategies*; Visconti, G., Carlo, P. D., Brune, W. H., Wahner, A., Schoeberl, M., Eds.; Springer: New York, NY, 2007; pp 230–237. https://doi.org/10.1007/978-0-387-35848-2_17.

(18) Turner, A. J.; Jacob, D. J. Balancing Aggregation and Smoothing Errors in Inverse Models. *Atmospheric Chemistry and Physics* **2015**, *15* (12), 7039–7048. https://doi.org/10.5194/acp-15-7039-2015.

(19) Cohen, J. B.; Wang, C. Estimating Global Black Carbon Emissions Using a Top-down Kalman Filter Approach. *Journal of Geophysical Research: Atmospheres* **2014**, *119* (1), 307–323. https://doi.org/10.1002/2013JD019912.

(20) Wang, P.; Wang, H.; Wang, Y. Q.; Zhang, X. Y.; Gong, S. L.; Xue, M.; Zhou, C. H.; Liu, H. L.; An, X. Q.; Niu, T.; Cheng, Y. L. Inverse Modeling of Black Carbon Emissions over China

Using Ensemble Data Assimilation. *Atmospheric Chemistry and Physics* **2016**, *16* (2), 989–1002. https://doi.org/10.5194/acp-16-989-2016.

(21) Mao, Y. H.; Li, Q. B.; Henze, D. K.; Jiang, Z.; Jones, D. B. A.; Kopacz, M.; He, C.; Qi, L.; Gao, M.; Hao, W.-M.; Liou, K.-N. Estimates of Black Carbon Emissions in the Western United States Using the GEOS-Chem Adjoint Model. *Atmospheric Chemistry and Physics* **2015**, *15* (13), 7685–7702. https://doi.org/10.5194/acp-15-7685-2015.

(22) Bao, F.; Cheng, T.; Li, Y.; Gu, X.; Guo, H.; Wu, Y.; Wang, Y.; Gao, J. Retrieval of Black Carbon Aerosol Surface Concentration Using Satellite Remote Sensing Observations. *Remote Sensing of Environment* **2019**, *226*, 93–108. https://doi.org/10.1016/j.rse.2019.03.036.

(23) Konovalov, I. B.; Lvova, D. A.; Beekmann, M.; Jethva, H.; Mikhailov, E. F.; Paris, J.-D.; Belan, B. D.; Kozlov, V. S.; Ciais, P.; Andreae, M. O. Estimation of Black Carbon Emissions from Siberian Fires Using Satellite Observations of Absorption and Extinction Optical Depths. *Atmospheric Chemistry and Physics* **2018**, *18* (20), 14889–14924. https://doi.org/10.5194/acp-18-14889-2018.

(24) McDuffie, E. E.; Smith, S. J.; O'Rourke, P.; Tibrewal, K.; Venkataraman, C.; Marais, E. A.; Zheng, B.; Crippa, M.; Brauer, M.; Martin, R. V. A Global Anthropogenic Emission Inventory of Atmospheric Pollutants from Sector- and Fuel-Specific Sources (1970–2017): An Application of the Community Emissions Data System (CEDS). *Earth System Science Data* **2020**, *12* (4), 3413–3442. https://doi.org/10.5194/essd-12-3413-2020.

(25) Ren, Y.; Oxford, C. R.; Zhang, D.; Liu, X.; Zhu, H.; Dillner, A. M.; White, W. H.; Chakrabarty, R. K.; Hasheminassab, S.; Diner, D. J.; Le Roy, E. J.; Kumar, J.; Viteri, V.; Song, K.; Akoshile, C.; Amador-Muñoz, O.; Asfaw, A.; Chang, R. Y.-W.; Francis, D.; Gahungu, P.; Garland, R. M.; Grutter, M.; Kim, J.; Langerman, K.; Lee, P.-C.; Lestari, P.; Mayol-Bracero, O. L.; Naidoo, M.; Nelli, N.; O'Neill, N.; Park, S. S.; Salam, A.; Sarangi, B.; Schechner, Y.; Schofield, R.; Tripathi, S. N.; Windwer, E.; Wu, M.-T.; Zhang, Q.; Rudich, Y.; Brauer, M.; Martin, R. V. Black Carbon Emissions Generally Underestimated in the Global South as Revealed by Globally Distributed Measurements. *Nat Commun* **2025**, *16* (1), 7010. https://doi.org/10.1038/s41467-025-62468-5.

(26) Klimont, Z.; Kupiainen, K.; Heyes, C.; Purohit, P.; Cofala, J.; Rafaj, P.; Borken-Kleefeld, J.; Schöpp, W. Global Anthropogenic Emissions of Particulate Matter Including Black Carbon. *Atmospheric Chemistry and Physics* **2017**, *17* (14), 8681–8723. https://doi.org/10.5194/acp-17-8681-2017.

(27) Briggs, N. L.; Long, C. M. Critical Review of Black Carbon and Elemental Carbon Source Apportionment in Europe and the United States. *Atmospheric Environment* **2016**, *144*, 409–427. https://doi.org/10.1016/j.atmosenv.2016.09.002.

(28) McDonald, B. C.; Goldstein, A. H.; Harley, R. A. Long-Term Trends in California Mobile Source Emissions and Ambient Concentrations of Black Carbon and Organic Aerosol. *Environ. Sci. Technol.* **2015**, *49* (8), 5178–5188. https://doi.org/10.1021/es505912b.

(29) Air Quality System Database. https://aqs.epa.gov/aqsweb/airdata/download_files.html#Meta.

(30) Spada, N. J.; Hyslop, N. P. Comparison of Elemental and Organic Carbon Measurements between IMPROVE and CSN before and after Method Transitions. *Atmospheric Environment* **2018**, *178*, 173–180. https://doi.org/10.1016/j.atmosenv.2018.01.043.

(31) Zhang, X.; Trzepla, K.; White, W.; Raffuse, S.; Hyslop, N. P. Intercomparison of Thermal–Optical Carbon Measurements by Sunset and Desert Research Institute (DRI) Analyzers Using the IMPROVE_A Protocol. *Atmospheric Measurement Techniques* **2021**, *14* (5), 3217–3231. https://doi.org/10.5194/amt-14-3217-2021.

(32) Coats, J.; Houyoux, M. R. Fast Emissions Modeling with the Sparse Matrix Operator Kernel Emissions (SMOKE) Modeling System. **1996**.

(33) Emissions Spatial and Temporal Allocator. https://github.com/mmb-carb/ESTA.

(34) California Fire Incidents Database. https://www.fire.ca.gov/incidents, accessed 2026-02-01.

(35) Ying, Q.; Feng, M.; Song, D.; Wu, L.; Hu, J.; Zhang, H.; Kleeman, M. J.; Li, X. Improve Regional Distribution and Source Apportionment of PM2.5 Trace Elements in China Using Inventory-Observation Constrained Emission Factors. *Science of The Total Environment* **2018**, *624*, 355–365. https://doi.org/10.1016/j.scitotenv.2017.12.138.

(36) Liao, K.; Zhang, J.; Chen, Y.; Lu, X.; Fung, J. C. H.; Ying, Q.; Yu, J. Z. Regional Source Apportionment of Trace Metals in Fine Particulate Matter Using an Observation-Constrained Hybrid Model. *npj Clim Atmos Sci* **2023**, *6* (1), 65. https://doi.org/10.1038/s41612-023-00393-4.

(37) Byun, D.; Schere, K. L. Review of the Governing Equations, Computational Algorithms, and Other Components of the Models-3 Community Multiscale Air Quality (CMAQ) Modeling System. *Appl. Mech. Rev* **2006**, *59* (2), 51–77. https://doi.org/10.1115/1.2128636.

(38) Xie, Y.; Paulot, F.; Carter, W. P. L.; Nolte, C. G.; Luecken, D. J.; Hutzell, W. T.; Wennberg, P. O.; Cohen, R. C.; Pinder, R. W. Understanding the Impact of Recent Advances in Isoprene Photooxidation on Simulations of Regional Air Quality. *Atmospheric Chemistry and Physics* **2013**, *13* (16), 8439–8455. https://doi.org/10.5194/acp-13-8439-2013.

(39) Mozart2CAMx Preprocessor. http://www.camx.com/download/support-software.aspx, accessed 2026-02-01.

(40) Community Atmosphere Model with Chemistry (CAM-CHEM) Outputs. https://www.acom.ucar.edu/cam-chem/cam-chem.shtml, accessed 2026-02-01.

(41) High-Resolution Rapid Refresh (HRRR) v4 Dataset. https://console.cloud.google.com/marketplace/product/noaa-public/hrrr?project=python-232920&pli=1.

(42) Emery, C.; Tai, E. Enhanced Meteorological Modeling and Performance Evaluation for Two Texas Ozone Episodes; 2001.

(43) Zhang, Y.; Liu, P.; Pun, B.; Seigneur, C. A Comprehensive Performance Evaluation of MM5-CMAQ for the Summer 1999 Southern Oxidants Study Episode—Part I: Evaluation Protocols, Databases, and Meteorological Predictions. *Atmospheric Environment* **2006**, *40* (26), 4825–4838. https://doi.org/10.1016/j.atmosenv.2005.12.043.

(44) McNally, D. 12km MM5 Performance Goals; 2009.

(45) Zhang, H.; Chen, G.; Hu, J.; Chen, S.-H.; Wiedinmyer, C.; Kleeman, M.; Ying, Q. Evaluation of a Seven-Year Air Quality Simulation Using the Weather Research and Forecasting (WRF)/Community Multiscale Air Quality (CMAQ) Models in the Eastern United States. *Science of The Total Environment* **2014**, *473–474*, 275–285. https://doi.org/10.1016/j.scitotenv.2013.11.121.

(46) Liao, K.; Park, E. S.; Zhang, J.; Cheng, L.; Ji, D.; Ying, Q.; Yu, J. Z. A Multiple Linear Regression Model with Multiplicative Log-Normal Error Term for Atmospheric Concentration Data. *Science of The Total Environment* **2021**, *767*, 144282. https://doi.org/10.1016/j.scitotenv.2020.144282.

(47) Chen, Z.; Jacob, D. J.; Nesser, H.; Sulprizio, M. P.; Lorente, A.; Varon, D. J.; Lu, X.; Shen, L.; Qu, Z.; Penn, E.; Yu, X. Methane Emissions from China: A High-Resolution Inversion of TROPOMI Satellite Observations. *Atmospheric Chemistry and Physics* **2022**, *22* (16), 10809–10826. https://doi.org/10.5194/acp-22-10809-2022.

(48) Cape, J. N.; Coyle, M.; Dumitrean, P. The Atmospheric Lifetime of Black Carbon. *Atmospheric Environment* **2012**, *59*, 256–263. https://doi.org/10.1016/j.atmosenv.2012.05.030.

(49) Lund, M. T.; Samset, B. H.; Skeie, R. B.; Watson-Parris, D.; Katich, J. M.; Schwarz, J. P.; Weinzierl, B. Short Black Carbon Lifetime Inferred from a Global Set of Aircraft Observations. *npj Clim Atmos Sci* **2018**, *1* (1), 31. https://doi.org/10.1038/s41612-018-0040-x.

(50) Boylan, J. W.; Russell, A. G. PM and Light Extinction Model Performance Metrics, Goals, and Criteria for Three-Dimensional Air Quality Models. *Atmospheric Environment* **2006**, *40* (26), 4946–4959. https://doi.org/10.1016/j.atmosenv.2005.09.087.

(51) Johnson, T. V. Review of Diesel Emissions and Control. *International Journal of Engine Research* **2009**, *10* (5), 275–285. https://doi.org/10.1243/14680874JER04009.

(52) Millstein, D. E.; Harley, R. A. Effects of Retrofitting Emission Control Systems on In-Use Heavy Diesel Vehicles. *Environ. Sci. Technol.* **2010**, *44* (13), 5042–5048. https://doi.org/10.1021/es1006669.

(53) Ruehl, C.; Misra, C.; Yoon, S.; Smith, J. D.; Burnitzki, M.; Hu, S.; Collins, J.; Tan, Y.; Huai, T.; Herner, J. Evaluation of Heavy-Duty Vehicle Emission Controls with a Decade of California Real-World Observations. *Journal of the Air & Waste Management Association* **2021**, *71* (10), 1277–1291. https://doi.org/10.1080/10962247.2021.1890277.

(54) US Census Bureau. TIGER/Line 2020 California Shapefiles. https://catalog.data.gov/dataset/tiger-line-shapefile-2020-state-california-2020-census-block.

(55) Brown, S. G.; Hyslop, N. P.; Roberts, P. T.; McCarthy, M. C.; Lurmann, F. W. Wintertime Vertical Variations in Particulate Matter (PM) and Precursor Concentrations in the San Joaquin Valley during the California Regional Coarse PM/Fine PM Air Quality Study. *Journal of the Air & Waste Management Association* **2006**, *56* (9), 1267–1277. https://doi.org/10.1080/10473289.2006.10464583.

(56) MacDonald, C. P.; McCarthy, M. C.; Dye, T. S.; Wheeler, N. J. M.; Hafner, H. R.; Roberts, P. T. Transport and Dispersion during Wintertime Particulate Matter Episodes in the San Joaquin Valley, California. *Journal of the Air & Waste Management Association* **2006**, *56* (7), 961–976. https://doi.org/10.1080/10473289.2006.10464509.

(57) Kirchstetter, T. W.; Corrigan, C. E.; Novakov, T. Laboratory and Field Investigation of the Adsorption of Gaseous Organic Compounds onto Quartz Filters. *Atmospheric Environment* **2001**, *35* (9), 1663–1671. https://doi.org/10.1016/S1352-2310(00)00448-9.

(58) Yang, H.; Yu, J. Z. Uncertainties in Charring Correction in the Analysis of Elemental and Organic Carbon in Atmospheric Particles by Thermal/Optical Methods. *Environ Sci Technol* **2002**, *36* (23), 5199–5204. https://doi.org/10.1021/es025672z.

(59) Bond, T. C.; Streets, D. G.; Yarber, K. F.; Nelson, S. M.; Woo, J.-H.; Klimont, Z. A Technology-Based Global Inventory of Black and Organic Carbon Emissions from Combustion. *Journal of Geophysical Research: Atmospheres* **2004**, *109* (D14). https://doi.org/10.1029/2003JD003697.

(60) Chow, J. C.; Watson, J. G.; Lowenthal, D. H.; Chen, L.-W. A.; Motallebi, N. Black and Organic Carbon Emission Inventories: Review and Application to California. *Journal of the Air & Waste Management Association* **2010**, *60* (4), 497–507. https://doi.org/10.3155/1047-3289.60.4.497.

(61) Chow, J. C.; Watson, J. G.; Lowenthal, D. H.; Antony Chen, L.-W.; Motallebi, N. PM2.5 Source Profiles for Black and Organic Carbon Emission Inventories. *Atmospheric Environment* **2011**, *45* (31), 5407–5414. https://doi.org/10.1016/j.atmosenv.2011.07.011.

(62) Chow, J. C.; Watson, J. G.; Lowenthal, D. H.; Chen, L.-W. A. *Climate Change – Characterization of Black Carbon and Organic Carbon Air Pollution Emissions and Evaluation of Measurement Methods. Phase II: Characterization of Black Carbon and Organic Carbon Source Emissions.*

(63) May, A. A.; Nguyen, N. T.; Presto, A. A.; Gordon, T. D.; Lipsky, E. M.; Karve, M.; Gutierrez, A.; Robertson, W. H.; Zhang, M.; Brandow, C.; Chang, O.; Chen, S.; Cicero-Fernandez, P.; Dinkins, L.; Fuentes, M.; Huang, S.-M.; Ling, R.; Long, J.; Maddox, C.; Massetti, J.; McCauley, E.; Miguel, A.; Na, K.; Ong, R.; Pang, Y.; Rieger, P.; Sax, T.; Truong, T.; Vo, T.; Chattopadhyay, S.; Maldonado, H.; Maricq, M. M.; Robinson, A. L. Gas- and Particle-Phase

Primary Emissions from in-Use, on-Road Gasoline and Diesel Vehicles. *Atmospheric Environment* **2014**, *88*, 247–260. https://doi.org/10.1016/j.atmosenv.2014.01.046.

(64) Sonntag, D. B.; Baldauf, R. W.; Yanca, C. A.; Fulper, C. R. Particulate Matter Speciation Profiles for Light-Duty Gasoline Vehicles in the United States. *Journal of the Air & Waste Management Association* **2014**, *64* (5), 529–545. https://doi.org/10.1080/10962247.2013.870096.

(65) Ban-Weiss, G. A.; McLaughlin, J. P.; Harley, R. A.; Lunden, M. M.; Kirchstetter, T. W.; Kean, A. J.; Strawa, A. W.; Stevenson, E. D.; Kendall, G. R. Long-Term Changes in Emissions of Nitrogen Oxides and Particulate Matter from on-Road Gasoline and Diesel Vehicles. *Atmospheric Environment* **2008**, *42* (2), 220–232. https://doi.org/10.1016/j.atmosenv.2007.09.049.

(66) Khalek, I. A.; Bougher, T. L.; Merritt, P. M.; Zielinska, B. Regulated and Unregulated Emissions from Highway Heavy-Duty Diesel Engines Complying with U.S. Environmental Protection Agency 2007 Emissions Standards. *Journal of the Air & Waste Management Association* **2011**, *61* (4), 427–442. https://doi.org/10.3155/1047-3289.61.4.427.

(67) Khalek, I. A.; Blanks, M. G.; Merritt, P. M.; Zielinska, B. Regulated and Unregulated Emissions from Modern 2010 Emissions-Compliant Heavy-Duty on-Highway Diesel Engines. *Journal of the Air & Waste Management Association* **2015**, *65* (8), 987–1001. https://doi.org/10.1080/10962247.2015.1051606.

(68) Manchanda, C.; Harley, R.; Marshall, J.; Turner, A.; Apte, J. Integrating Mobile and Fixed-Site Black Carbon Measurements to Bridge Spatiotemporal Gaps in Urban Air Quality. *ChemRxiv 2023* (1226). https://doi.org/10.26434/chemrxiv-2023-d4q7n.

(69) Currie, L. A.; Benner, B. A.; Kessler, J. D.; Klinedinst, D. B.; Klouda, G. A.; Marolf, J. V.; Slater, J. F.; Wise, S. A.; Cachier, H.; Cary, R.; Chow, J. C.; Watson, J.; Druffel, E. R. M.; Masiello, C. A.; Eglinton, T. I.; Pearson, A.; Reddy, C. M.; Gustafsson, Ö.; Quinn, J. G.; Hartmann, P. C.; Hedges, J. I.; Prentice, K. M.; Kirchstetter, T. W.; Novakow, T.; Puxbaum, H.; Schmid, H. A Critical Evaluation of Interlaboratory Data on Total, Elemental, and Isotopic Carbon in the Carbonaceous Particle Reference Material, NIST SRM 1649a. *J Res Natl Inst Stand Technol* **2002**, *107* (3), 279–298. https://doi.org/10.6028/jres.107.022.

(70) Cheng, Y.; He, K. B.; Duan, F. K.; Zheng, M.; Ma, Y. L.; Tan, J. H. Positive Sampling Artifact of Carbonaceous Aerosols and Its Influence on the Thermal-Optical Split of OC/EC. *Atmospheric Chemistry and Physics* **2009**, *9* (18), 7243–7256. https://doi.org/10.5194/acp-9-7243-2009.

(71) Wu, C.; Yu, J. Z. Determination of Primary Combustion Source Organic Carbon-to-Elemental Carbon (OC / EC) Ratio Using Ambient OC and EC Measurements: Secondary OC-EC Correlation Minimization Method. *Atmospheric Chemistry and Physics* **2016**, *16* (8), 5453–5465. https://doi.org/10.5194/acp-16-5453-2016.

(72) Khan, B.; Hays, M. D.; Geron, C.; Jetter, J. Differences in the OC/EC Ratios That Characterize Ambient and Source Aerosols Due to Thermal-Optical Analysis. *Aerosol Science and Technology* **2012**, *46* (2), 127–137. https://doi.org/10.1080/02786826.2011.609194.

(73) Jaffrezo, J.-L.; Aymoz, G.; Cozic, J. Size Distribution of EC and OC in the Aerosol of Alpine Valleys during Summer and Winter. *Atmospheric Chemistry and Physics* **2005**, *5* (11), 2915–2925. https://doi.org/10.5194/acp-5-2915-2005.

(74) Karanasiou, A.; Minguillón, M. C.; Viana, M.; Alastuey, A.; Putaud, J.-P.; Maenhaut, W.; Panteliadis, P.; Močnik, G.; Favez, O.; Kuhlbusch, T. a. J. Thermal-Optical Analysis for the Measurement of Elemental Carbon (EC) and Organic Carbon (OC) in Ambient Air a Literature Review. *Atmospheric Measurement Techniques Discussions* **2015**, *8* (9), 9649–9712. https://doi.org/10.5194/amtd-8-9649-2015.

797 Table of Content Graphic:

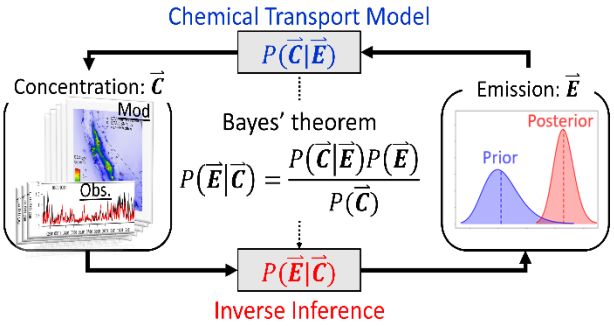

798

799